Monthly Notices of the ROYAL ASTRONOMICAL SOCIETY
MNRAS **497,** 4423–4435 (2020)
Advance Access publication 2020 July 17
doi:10.1093/mnras/staa2077

K2-280 b – a low density warm sub-Saturn around a mildly evolved star

Grzegorz Nowak,[1,2★] Enric Palle,[1,2] Davide Gandolfi,[3] Hans J. Deeg,[1,2] Teruyuki Hirano,[4] Oscar Barragán,[5,3] Masayuki Kuzuhara,[6,7] Fei Dai,[8,9] Rafael Luque,[1,2] Carina M. Persson,[10] Malcolm Fridlund,[10,11] Marshall C. Johnson,[12] Judith Korth,[13] John H. Livingston,[14] Sascha Grziwa,[13] Savita Mathur,[1,2] Artie P. Hatzes,[15] Jorge Prieto-Arranz,[1,2] David Nespral,[1,2] Diego Hidalgo,[1,2] Maria Hjorth,[16] Simon Albrecht,[16] Vincent Van Eylen,[8] Kristine W. F. Lam,[17] William D. Cochran,[18,19] Massimiliano Esposito,[15] Szilárd Csizmadia,[20] Eike W. Guenther,[15] Petr Kabath,[21] Pere Blay,[22] Rafael Brahm,[23,24] Andrés Jordán,[23,24] Néstor Espinoza,[25] Felipe Rojas,[26,24] Núria Casasayas Barris,[1,2] Florian Rodler,[27] Roi Alonso Sobrino,[1,2] Juan Cabrera,[20] Ilaria Carleo,[28] Alexander Chaushev,[17] Jerome de Leon,[14] Philipp Eigmüller,[20] Michael Endl,[19] Anders Erikson,[20] Akihiko Fukui,[7] Iskra Georgieva,[10] Lucía González-Cuesta,[1,2] Emil Knudstrup,[16] Mikkel N. Lund,[16] Pilar Montañes Rodríguez,[1,2] Felipe Murgas,[1,2] Norio Narita,[1,6,7,29] Prajwal Niraula,[30] Martin Pätzold,[13] Heike Rauer,[20,17] Seth Redfield,[28] Ignasi Ribas,[31,32] Marek Skarka,[21,33] Alexis M. S. Smith[20] and Jano Subjak[21,34]

Affiliations are listed at the end of the paper

Accepted 2020 July 8. Received 2020 July 7; in original form 2019 July 8

ABSTRACT

We present an independent discovery and detailed characterization of K2-280 b, a transiting low density warm sub-Saturn in a 19.9-d moderately eccentric orbit ($e = 0.35^{+0.05}_{-0.04}$) from *K2* campaign 7. A joint analysis of high precision HARPS, HARPS-N, and FIES radial velocity measurements and *K2* photometric data indicates that K2-280 b has a radius of $R_\mathrm{b} = 7.50 \pm 0.44$ $\mathrm{R}_\oplus$ and a mass of $M_\mathrm{b} = 37.1 \pm 5.6$ $\mathrm{M}_\oplus$, yielding a mean density of $\rho_\mathrm{b} = 0.48^{+0.13}_{-0.10}$ g cm^{-3}. The host star is a mildly evolved G7 star with an effective temperature of $T_\mathrm{eff} = 5500 \pm 100$ K, a surface gravity of $\log\, g_\star = 4.21 \pm 0.05$ (cgs), and an iron abundance of [Fe/H] $= 0.33 \pm 0.08$ dex, and with an inferred mass of $M_\star = 1.03 \pm 0.03$ $\mathrm{M}_\odot$ and a radius of $R_\star = 1.28 \pm 0.07$ $\mathrm{R}_\odot$. We discuss the importance of K2-280 b for testing formation scenarios of sub-Saturn planets and the current sample of this intriguing group of planets that are absent in the Solar system.

Key words: techniques: photometric – techniques: radial velocities – techniques: spectroscopic – planets and satellites: detection – stars: individual: (EPIC 216494238, K2-280).

1 INTRODUCTION

The main advantage of the extended NASA's *Kepler* mission (Borucki et al. 2010), known as *K2* (Howell et al. 2014), was a much larger number of bright stars in its fields of view located along the ecliptic. A significant number of planets transiting bright stars have been discovered in all *K2* campaigns (e.g. Montet et al. 2015; Crossfield et al. 2016; Vanderburg et al. 2016; Dressing et al. 2017; Crossfield et al. 2018; Livingston et al. 2018; Mayo et al. 2018; Petigura et al. 2018; Yu et al. 2018a). Some of these planets were only validated, but many were characterized by means of high precision radial velocity (RV) measurements that enabled mass determination with precision better than 20 per cent (e.g. Vanderburg et al. 2015; Christiansen et al. 2017; Gandolfi et al. 2017; Malavolta et al. 2018; Prieto-Arranz et al. 2018; Rodriguez et al. 2018; Barragán et al. 2018b). However much higher precision is needed to distinguish between various possible planetary compositions (see e.g. Dorn et al. 2015, and references therein). Mass determination with such precision for small planets ($R_\mathrm{p} = 1$–$4\,\mathrm{R}_\oplus$) were possible only for short period ($P_\mathrm{orb} \lesssim 10$ d) sub-Neptunes and super-Earths, which induces RV semi-amplitudes on the parent stars of a few m s^{-1}, and for stars hosting ultra-short period planets, for which the Doppler reflex motion is enhanced by the extremely short orbital period ($P_\mathrm{orb} < 1$ d; Winn, Sanchis-Ojeda & Rappaport 2018, and references therein). Most of the small *K2* planets with precise mass determination orbit bright stars, i.e. stars brighter than $V = 11.5$, which is the current limit for $\sim$1 m s^{-1} precision with spectrographs mounted at 3–4-m class telescopes (Pepe et al. 2013). The constraints for precise determination of planetary masses are naturally more relaxed for higher-mass planets, enabling us to study super-Neptune/sub-Saturn planets ($R_\mathrm{p} = 4$–$8\,\mathrm{R}_\oplus$) with longer orbital periods around fainter stars.

Sub-Saturns form a very intriguing group of planets that have no counterpart in the Solar System. Their main characteristic is a significant contribution of both heavy metal cores and low density

★ E-mail: gnowak@iac.es

© 2020 The Author(s)
Published by Oxford University Press on behalf of the Royal Astronomical Society

Downloaded from https://academic.oup.com/mnras/article/497/4/4423/5873020 by University College London user on 25 September 2020

gaseous envelopes to the total planet mass (Petigura et al. 2016). They are thus important laboratories to study envelope accretion. As shown by Petigura et al. (2017), the population of sub-Saturns has a very uniform distribution of the planetary mass between ∼6 and 60 $M_\oplus$. Similar to gas-giant planets, they are also found to orbit mainly metal-rich stars. Finally, the most massive sub-Saturns are often the only detected planet in the system and orbit their parent stars on eccentric orbits, which suggests that dynamical instability might have played an important role in their formation.

Here we present an independent discovery and characterisation of a low mass, sub-Saturn planet on a 20-d orbit around a relatively faint ($V = 12.5$), metal rich ($[Fe/H] = 0.33 \pm 0.08$ dex), slightly evolved *K2* star that was proposed as a planet candidate by Petigura et al. (2018) and Mayo et al. (2018), and statistically validated as a planet by Livingston et al. (2018). This kind of planets was usually avoided by RV follow-up of *K2* candidates because of the faintness of their host stars. Besides, slightly evolved stars are typically avoided in RV follow-up projects, because of their higher expected stellar jitter (see e.g. Hekker et al. 2006, 2008; Tayar, Stassun & Corsaro 2019, and references therein). Both these effects may bias the statistical analysis of warm-giant planets. K2-280 b joins a sample of 30 sub-Saturns with mean densities determined with precision better than 50 per cent discovered mainly by *Kepler* and *K2* (see Petigura et al. 2017, and references therein for first 23 planets).

This work was done as a part of the KESPRINT collaboration,[1] which aims to confirm and characterize *K2* and *TESS* planets. In Section 2, we describe the observations of K2-280, specifically the *K2* photometry, the NOT/FIES, ESO/HARPS, and TNG/HARPS-N high-resolution spectroscopy follow-up, and the high-contrast imaging. In Section 3 and 4, we present the properties of the host star K2-280 and the global analysis of photometric and Doppler data, respectively. In Section 5, we finally summarize and discuss the characteristics of K2-280 b in the context of the properties of the known population of sub-Saturn planets with mean densities determined with precision better than 50 per cent.

2 OBSERVATIONS AND DATA REDUCTIONS

2.1 *K2* Photometry

K2-280 was one of 13 469 long cadence targets observed from October 4th to December 26th 2015 (UT) during *K2* campaign 7. It was proposed as a target by GO programmes 7030 (PI Howard), and 7085 (PI Burke). We downloaded K2-280 images from the MAST archive[2] and used them to produce a de-trended *K2* light curve as described in detail in Dai et al. (2017). Fig. 1 shows the pixel mask used to perform simple aperture photometry. We used the box fitting least-square (BLS) routine (Kovács, Zucker & Mazeh 2002; Jenkins et al. 2010), improved by implementation of the optimal frequency sampling described in Ofir (2014) to search for transiting planet candidates in all Field 7 targets light curves. We detected transits of K2-280 b with a signal-to-noise ratio (SNR) of 24.5, depth of $\sim 3.5 \times 10^{-3}$, period of $P = 19.89518 \pm 0.00028$ d, and a mid-time of the first transit $T_0 = 2457\,307.581\,01 \pm 0.000\,59$ d in Barycentric Julian Date in the Barycentric Dynamical Time (BJD_{TDB}; see e.g. Eastman, Siverd & Gaudi 2010). The de-trended light curve of K2-280 with the correction for baseline flux variations and centroid motions is presented in Fig. 2 with the 4 transits observed by *K2* highlighted with red lines. We removed the baseline flux variation by fitting a spline function with a width of 3 d. In Table 1, we report the main identifiers of K2-280, along with its equatorial coordinates, space motion, distance, and optical and near-infrared magnitudes.

[1] https://www.iac.es/proyecto/kesprint/
[2] https://archive.stsci.edu/k2/data_search/search.php

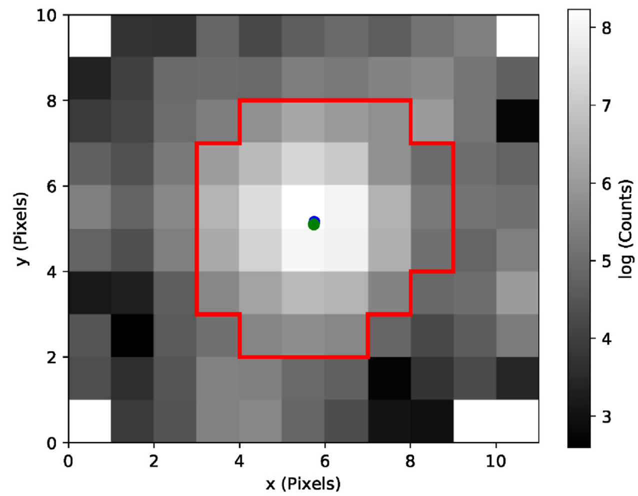

Figure 1. *K2* image of K2-280. Red lines show the aperture defined by the amount of light of each pixel and level of background light. The electron count is indicated by the intensity of shading (light grey for high and dark grey for low count). The green circle indicates the current position of the target in the EPIC catalogue, and the blue circle is the centre of the flux distribution. The scale of the image is the *Kepler* pixel scale of 3.98 arcsec pix^{-1}. The K2 image is not a rectangle, but it is irregularly shaped. The white pixels in the corners contain no data.

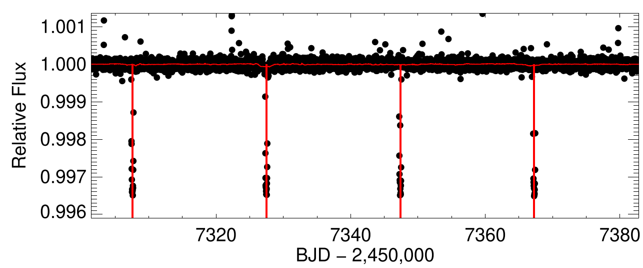

Figure 2. Detrended *K2* light curve of K2-280. The four transits observed by *K2* are marked by vertical solid red lines. The horizontal red line is the local median flux level with a window of 0.5 d.

2.2 High-dispersion spectroscopy

High-dispersion spectroscopic observations of K2-280 were obtained between 2016 April 30th (UT) and 2019 May 7th (UT) using ESO/HARPS, TNG/HARPS-N, and NOT/FIES spectrographs. We collected a total of 18 HARPS, 14 HARPS-N, and 6 FIES spectra. The details of these observations are given in the subsections below. Table 2 gives the time stamps of the spectra in BJD_{TDB}, the RVs along with their 1σ error bars, as well as the bisector inverse slope (BIS) and full-width at half maximum (FWHM) of the cross-correlation function (CCF).

2.2.1 *ESO/HARPS*

We started the RV follow-up of K2-280 using the High Accuracy Radial velocity Planet Searcher (HARPS) spectrograph ($R \approx 115\,000$,

Downloaded from https://academic.oup.com/mnras/article/497/4/4423/5873020 by University College London user on 25 September 2020

Table 1. Properties of K2-280.

Parameter	Value	Source
	Coordinates and main identifiers	
RA 2000.0 (h)	19:26:22.881	*Gaia* DR2
Dec 2000.0 (deg)	−22:14:51.552	*Gaia* DR2
Gaia DR2 identifier	6772454416893148928	*Gaia* DR2
2MASS identifier	19262288-2214514	2MASS PSC
UCAC identifier	339-184113	UCAC4
EPIC identifier	216494238	EPIC
TIC identifier	119605900	TIC
	Optical and near-infrared magnitudes	
K_p (mag)	12.302	*K2* EPIC
B (mag)	13.269 ± 0.010	UCAC4
V (mag)	12.536 ± 0.040	UCAC4
R (mag)	12.41 ± 0.07	UCAC4
G (mag)	12.3604 ± 0.0002	*Gaia* DR2
g (mag)	12.850 ± 0.020	UCAC4
r (mag)	12.320 ± 0.020	UCAC4
i (mag)	12.067 ± 0.040	UCAC4
J (mag)	11.141 ± 0.021	2MASS
H (mag)	10.854 ± 0.024	2MASS
K (mag)	10.765 ± 0.019	2MASS
	Space motion and distance	
$\mathrm{PM_{RA}}$ (mas yr^{-1})	4.44 ± 0.08	*Gaia* DR2
$\mathrm{PM_{Dec.}}$ (mas yr^{-1})	-12.50 ± 0.07	*Gaia* DR2
$\mathrm{RV}_{\gamma,\,\mathrm{HARPS}}$ (km s^{-1})	$-1.1934^{+0.0011}_{-0.0011}$	This work
$\mathrm{RV}_{\gamma,\,\mathrm{HARPS\text{-}N}}$ (km s^{-1})	$-1.1907^{+0.0011}_{-0.0011}$	This work
$\mathrm{RV}_{\gamma,\,\mathrm{FIES}}$ (km s^{-1})	$-1.2349^{+0.0038}_{-0.0039}$	This work
$\pi_\star$(mas)	2.526 ± 0.111	*Gaia* DR2
$d_\star$(pc)	$391.5^{+7.5}_{-7.2}$	Bailer-Jones et al. (2018)
U (km s^{-1})	-7.78 ± 0.06	This work
V (km s^{-1})	-5.98 ± 0.84	This work
W (km s^{-1})	-9.18 ± 0.71	This work
	Photospheric parameters	
T_{eff} (K)	5500 ± 100	This work
$\log\ g_\star{}^{(a)}$ (dex)	4.00 ± 0.10	This work
$\log\ g_\star{}^{(b)}$ (dex)	4.21 ± 0.05	This work
[Fe/H] (dex)	0.33 ± 0.08	This work
	Derived physical parameters	
$M_\star$ ($\mathrm{M_\odot}$)	1.03 ± 0.03	This work
$R_\star$ ($\mathrm{R_\odot}$)	1.28 ± 0.07	This work
$\rho_\star$ (g cm^{-3})	$0.8^{+0.16}_{-0.13}$	This work
Age (Gyr)	8.96 ± 1.70	This work
	Stellar rotation	
$v_{\mathrm{rot}}\sin i_\star$ (km s^{-1})	3.0 ± 1.0	This work

Notes. [a]From spectroscopy.
[b]From stellar mass and radius.

Mayor et al. 2003) mounted at the ESO 3.57-m telescope of La Silla Observatory in Chile. We acquired 18 spectra between 2016 April 30th (UT) and 2018 April 27th 2018 (UT) under the observing programmes 097.C-0571(B), 097.C-0948(A), 098.C-0860(A), 099.C-0491(A), 0101.C-0407(A), and 60.A-9700(G), setting the exposure times to 1200–3600 s. The dedicated on-line HARPS Data Reduction Software (DRS) was used to reduce the spectra, and extract the Doppler measurements and spectral activity indicators. The SNR per pixel at 5500 Å is in the range 22–46. RVs were measured by cross-correlating the extracted spectra with a G2 numerical mask (Baranne et al. 1996). The uncertainties of the measured RVs are in the range 2.1–8.1 m s^{-1} with a mean value of 4.2 m s^{-1}.

Table 2. HARPS, HARPS-N, and FIES radial velocities (RVs), BIS, and FWHM of the CCF.

$\mathrm{BJD_{TDB}}$ −2450 000	RV (m s^{-1})	σ_{RV} (m s^{-1})	BIS (m s^{-1})	σ_{BIS} (m s^{-1})	FWHM (km s^{-1})
FIES					
7566.606106	−1236.447	10.145	−25.604	8.240	12.240
7570.575852	−1248.492	8.236	−19.745	5.424	12.237
7579.594362	−1221.025	13.568	−15.325	10.160	12.257
7583.604507	−1227.357	11.149	−1.138	9.710	12.232
7600.515019	−1233.204	8.028	−36.207	7.614	12.283
7638.387601	−1225.100	6.816	−23.315	4.940	12.220
HARPS-N					
7585.595242	−1192.158	6.794	−15.933	9.608	7.354
7603.514891	−1191.265	5.126	−13.175	7.249	7.363
7611.572851	−1201.759	8.653	−15.272	12.238	7.371
7892.699273	−1195.302	3.475	−5.393	4.915	7.348
7921.702566	−1191.619	3.014	−7.642	4.263	7.359
7958.534636	−1194.254	7.553	−39.517	10.682	7.360
7965.540153	−1197.765	2.357	−14.982	3.334	7.360
8013.363503	−1186.028	1.991	−18.747	2.816	7.366
8013.404784	−1185.686	2.117	−30.544	2.994	7.362
8014.362082	−1185.942	2.722	−28.539	3.850	7.352
8014.402379	−1189.116	2.756	−24.429	3.898	7.365
8015.359376	−1178.088	5.620	−11.056	7.948	7.349
8015.402150	−1187.664	5.605	−13.530	7.927	7.368
8610.724187	−1193.898	4.651	−17.515	6.577	7.359
HARPS					
7508.854151	−1195.313	3.185	−5.317	4.504	7.447
7511.892058	−1194.114	4.462	−2.236	6.310	7.409
7609.625616	−1195.440	2.732	19.011	3.865	7.415
7619.566531	−1184.749	4.551	16.474	6.437	7.413
7637.587335	−1181.617	6.366	−13.161	9.004	7.400
7638.596015	−1172.262	7.600	−21.324	10.748	7.447
7639.571271	−1181.987	6.990	−34.526	9.885	7.389
7645.538147	−1194.348	4.671	11.465	6.607	7.433
7682.520265	−1194.190	5.191	17.641	7.342	7.420
7984.617196	−1190.758	2.370	−5.857	3.352	7.422
7986.590931	−1203.107	3.223	−1.852	4.559	7.421
7987.587443	−1197.553	2.285	13.255	3.232	7.415
7990.553698	−1195.977	2.729	24.528	3.859	7.418
7990.593359	−1207.601	2.817	−20.535	3.983	7.396
7992.576732	−1189.811	2.093	16.287	2.950	7.419
7992.609762	−1187.701	2.759	−9.069	3.902	7.408
8003.594697	−1191.639	3.620	−0.841	5.110	7.401
8235.876739	−1189.777	8.100	−22.636	11.455	7.409

2.2.2 *TNG/HARPS-N*

Between 2016 July 16th (UT) and 2019 May 7th (UT) we collected 14 spectra with the HARPS-N spectrograph ($R \approx 115\,000$, Cosentino et al. 2012) mounted at the 3.58-m Telescopio Nazionale Galileo (TNG) of Roque de los Muchachos Observatory in La Palma, Spain, under the observing programmes A33TAC_15, OPT17A_64, CAT17A_91, and CAT19A_97. The exposure time was set to 1200–3600, based on weather conditions and scheduling constraints, leading to an SNR per pixel of 15–47 at 5500 Å. The spectra were extracted using the off-line version of the HARPS-N DRS pipeline. Doppler measurements and spectral activity indicators were measured using an on-line version of the DRS, the YABI tool,[3] by cross-correlating the extracted spectra with a G2 mask (Baranne

[3]Available at http://ia2-harps.oats.inaf.it:8000.

Downloaded from https://academic.oup.com/mnras/article/497/4/4423/5873020 by University College London user on 25 September 2020

et al. 1996). The uncertainty of the measured RVs is in the range 2.0–8.6 m s^{-1}, with a mean value of 4.5 m s^{-1}.

2.2.3 NOT/FIES

We acquired 6 additional spectra using the FIbre-fed Échelle Spectrograph (FIES; Frandsen & Lindberg 1999; Telting et al. 2014) mounted at the 2.56-m Nordic Optical Telescope (NOT) of Roque de los Muchachos Observatory (La Palma, Spain). The observations were carried out between 2016 June 26th and September 6th (UT), as part of the OPTICON observing programme 53-109. We used the FIES high-resolution mode, which provides a resolving power of $R = 67\,000$ in the spectral range 3700–7300 Å. Following the observing strategy described in Buchhave et al. (2010) and Gandolfi et al. (2015), we traced the RV drift of the instrument by acquiring long-exposed ThAr spectra ($T_{\rm exp} \approx 35$ s) immediately before and after each science exposure. The exposure time was set to 2700–3600 s, according to the sky conditions and scheduling constraints. The data reduction follows standard IRAF and IDL routines, which includes bias subtraction, flat fielding, order tracing and extraction, and wavelength calibration. Radial velocity measurements were computed via multi-order cross-correlations with the RV standard star HD 50692 (Udry, Mayor & Queloz 1999), observed with the same instrument set-up as K2-280. The SNR per pixel at 5500 Å of the extracted spectra is in the range 15–35. The uncertainties are in the range 6.8–13.6 m s^{-1} with a mean value of 9.7 m s^{-1}.

2.3 High contrast imaging

To search for nearby stars and estimate a potential contamination factor from such sources we used a high contrast image of K2-280 publicly available on the ExoFOP-K2 website.[4] The image was acquired on 2016 June 19th (UT) using the Frederick C. Gillett Gemini North telescope and its adaptive optics (AO) system facility, ALTAIR with a natural guide star along with a Near InfraRed Imager and spectrograph (NIRI; Hodapp et al. 2003) using the Brackett Gamma (Brγ) filter (Gemini-North ID G0218) centred at 2.17 µm, under Gemini Science Program GN-2016A-LP-5. Two faint stars are visible on the Gemini-North/NIRI+ALTAIR AO image of K2-280 (Fig. 3): a very close-in companion at ∼0.4 arcsec west–north-west (W–NW), and a distant source at ∼6.6″ south–south-east (S–SE) of K2-280. We carefully analyzed the Gemini-North/NIRI+ALTAIR AO image of K2-280. Table 3 reports separations, position angles, the magnitude difference $\Delta m_{\rm Br\gamma}$, and the $\Delta F_{\rm Br\gamma}$ flux-ratio of these two objects relative to K2-280. Their brightness ratio at 2.17 µm is comparable to the observed *K2* transit depth (3500 ppm), which requires their consideration as sources of false positives (see Section 3.5).

3 PROPERTIES OF THE HOST STAR

3.1 *Gaia* measurements

K2-280 is among a small sub-sample of ESA's *Gaia* mission (Gaia Collaboration 2016) targets for which the *Gaia* DR2 (Gaia Collaboration 2018)[5] – a first *Gaia*-only catalogue – provides not only astrometric measurements, but also astrophysical parameters (radii, luminosities, extinctions, and reddening) and median RVs. *Gaia* DR2 astrometric parameters of K2-280 are included in Table 1.

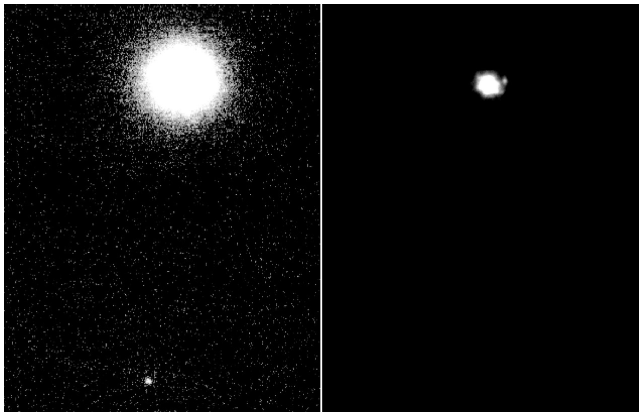

Figure 3. AO image of the surroundings of K2-280 obtained with the Gemini-North/NIRI+ALTAIR instrument. Both panels show the same image, with a field of view of 8.7 arcsec in the N–S and 6.7 arcsec in the E–W direction (north to the top and east to the left), but with different brightness scales. The left-hand panel shows the star at 6.6 arcsec in the S–SE direction and the right one the close neighbor at 0.4 arcsec W–NW of K2-280.

Table 3. Relative properties of the two nearby stars to K2-280 detected with the Gemini-North/NIRI+ALTAIR.

Parameter	W–NW Close-in star	S–SE Distant star
Separation (arcsec)	0.38 ± 0.011	6.598 ± 0.011
Position angle (deg)	286.2 ± 1.5	173.3 ± 1.5
$\Delta m_{\rm Br\gamma}$ (mag)	4.72 ± 0.15	6.65 ± 0.15
$\Delta F_{\rm Br\gamma}$ relative flux	$(1.3 \pm 0.2) \times 10^{-2}$	$(2.2 \pm 0.4) \times 10^{-3}$

Gaia DR2 values of stellar radius and median RV of K2-280 agree with the values determined in the subsections below.

3.2 Photospheric parameters and stellar rotation velocity measurements using SME

We followed the procedure described in Fridlund et al. (2017) and Persson et al. (2018) and analysed the co-added spectra from HARPS, HARPS-N, and FIES with the spectral analysis package Spectroscopy Made Easy (SME; Valenti & Piskunov 1996; Valenti & Fischer 2005; Piskunov & Valenti 2017) to derive the effective temperature $T_{\rm eff}$, surface gravity log $g_\star$, iron abundance [Fe/H], and projected rotational velocity $v_{\rm rot}\sin i_\star$. SME uses grids of atmosphere models to calculate synthetic stellar spectra, which are fitted to the observed spectra using a χ^2-minimizing procedure. We use the line wings of Hα, which is rather insensitive to log $g_\star$ for this spectral type, to model $T_{\rm eff}$ (with a fixed log $g_\star$), and the line wings of the Ca I triplet to model log $g_\star$ (with a fixed $T_{\rm eff}$). We used the latest version of the software (5.2.2) and line lists from the Vienna atomic line data base.[6] The model spectra were taken from ATLAS12 (Kurucz 2013). The calibration equations for Sun-like stars from Bruntt et al. (2010) and Doyle et al. (2014) were adopted to fix the micro- and macroturbulent velocities, $v_{\rm mic}$ and $v_{\rm mac}$ to 0.5 and 1.0 km s^{-1}, respectively. The spectroscopic parameters derived from the HARPS, HARPS-N, and FIES co-added spectra agree well within their nominal error bars. The final adopted values are $T_{\rm eff} = 5500 \pm 100$ K, log $g_\star = 4.00 \pm 0.10$ (cgs), and [Fe/H] =

[4]See https://exofop.ipac.caltech.edu/k2/edit_target.php?id=216494238.
[5]Released on 2018 April 25th.

[6]http://vald.astro.uu.se

Downloaded from https://academic.oup.com/mnras/article/497/4/4423/5873020 by University College London user on 25 September 2020

0.33 ± 0.08 dex (Table 1). They are defined as the weighted mean of the individual parameters derived from the HARPS, HARPS-N, and FIES co-added spectra.

3.3 Photospheric parameters and radius measurements using `SpecMatch-emp`

As a sanity check, we also analysed the co-added HARPS and HARPS-N spectra using the `SpecMatch-emp` software package (Yee, Petigura & von Braun 2017). `SpecMatch-emp` estimates the stellar effective temperature $T_{\rm eff}$, radius $R_\star$, and iron abundance [Fe/H] by fitting the spectral region between 5000 and 5900 Å to hundreds of library spectra gathered by the California Planet Search programme. Following the procedure described in Hirano et al. (2018), we reformatted the co-added HARPS and HARPS-N spectra so that they can be read by `SpecMatch-emp`. We found $T_{\rm eff} = 5597 \pm 110$ K and [Fe/H] $= 0.33 \pm 0.08$ dex, which agree with the effective temperature and iron abundance determined with SME (Table 1) within 1σ. We found also that K2-280 is a slightly evolved star with a stellar radius of $R_\star = 1.33 \pm 0.21\,{\rm R}_\oplus$. We finally obtained a first estimate of the stellar mass ($M_\star = 1.16 \pm 0.08\,{\rm M}_\oplus$) via Monte Carlo simulations using the empirical equations by Torres, Andersen & Giménez (2010) alongside $T_{\rm eff}$, [Fe/H], and $R_\star$.

3.4 Physical parameters

We refined the fundamental parameters of K2-280 utilising the web interface[7] `PARAM 1.3` along with `PARSEC` isochrones (Bressan et al. 2012). Following the method described in Gandolfi et al. (2008), we found that the interstellar extinction along the line of sight to the star is $A_{\rm v} = 0.10 \pm 0.05$. Using the effective temperature and iron abundance derived in Section 3.2, alongside the extinction-corrected visual magnitude and the *Gaia* parallax[8] (Table 1), we determined a mass of $M_\star = 1.03 \pm 0.03\,{\rm M}_\odot$ and a radius of $R_\star = 1.28 \pm 0.07\,{\rm R}_\odot$, which agree with the values derived in Section 3.3. Stellar mass and radius implies a surface gravity of $\log g_\star = 4.21 \pm 0.05$ (cgs), which is higher than our spectroscopic value of 4.0 ± 0.1 (cgs), but within its 2σ error bars. The age of the star was constrained to be 8.9 ± 1.7 Gyr, further confirming the evolved status of K2-280. The values of stellar radius and mass agree within 3σ with the ones determined by Petigura et al. (2018) ($R_\star = 1.45^{+0.20}_{-0.18}\,{\rm R}_\odot$, $M_\star = 1.17^{+0.10}_{-0.08}\,{\rm M}_\odot$), Mayo et al. (2018) ($R_\star = 1.064^{+0.069}_{-0.047}\,{\rm R}_\odot$, $M_\star = 1.101^{+0.025}_{-0.028}\,{\rm M}_\odot$), and Livingston et al. (2018) ($R_\star = 1.28 \pm 0.03\,{\rm R}_\odot$, $M_\star = 1.11 \pm 0.04\,{\rm M}_\odot$). We stress that the parameter estimates determined in the three works listed above are based on spectra with relatively low SNR, in contrast to our co-added, high SNR, HARPS, HARPS-N, and FIES spectra. Petigura et al. (2018) and Livingston et al. (2018) used the same spectra collected with the HIgh Resolution Echelle Spectrometer (HIRES; Vogt et al. 1994) mounted on 10-m Keck I telescope, with typical SNR = 45 for stars with $V < 13.0$. Mayo et al. (2018) used spectra collected with Tillinghast Reflector Echelle Spectrograph (TRES) mounted on the 1.5-m Tillinghast telescope at the Whipple Observatory on Mt. Hopkins in Arizona with even lower SNR.

We also calculated the *UVW* space velocities of K2-280 using the IDL code `gal_uvw`[9] (based upon Johnson & Soderblom 1987), using the *Gaia* DR2 proper motions and parallax, and the average of the HARPS and HARPS-N systemic velocities γ (Table 1). Our calculated values of *UVW* are listed in Table 1; we quote values in the local standard of rest using the solar motion of Coşkunoğlu et al. (2011). We then used the methodology of Reddy, Lambert & Allende Prieto (2006) to determine the Galactic population membership of K2-280. We found that K2-280 has a >99 per cent probability of belonging to the Galactic thin disc, and less than 1 per cent of belonging to either the thick disc or the halo. This is consistent with K2-280's high metallicity of [Fe/H] $= 0.33 \pm 0.08$ dex.

The final adopted stellar parameters are listed in Table 1. The effective temperature and surface gravity translate into a G7 V spectral type (Gray & Corbally 2009).

3.5 Faint AO companions

From the two faint companions to K2-280 identified in the Gemini-North/NIRI+ALTAIR AO image (Section 2.3), the one located 6.6 arcsec S–SE of K2-280 was identified in the *Gaia* DR2 as the source 6772454206445987712. Based on its very small proper motion (${\rm PM_{RA}} = 0.29 \pm 0.52$ mas yr^{-1} and ${\rm PM_{Dec.}} = -0.92 \pm 0.45$ mas yr^{-1}) and distance found by Bailer-Jones et al. (2018) ($d = 5.103^{+3.435}_{-2.094}$ kpc), we concluded that it is a background star. Using the *Gaia* *G*-band magnitude ($G = 18.765 \pm 0.010$), we derived a *G*-band brightness ratio relative to K2-280 of 0.0027 ± 0.0001. Considering the close similarity between the *Gaia G* band and the *Kepler* passband, this companion is too faint to be the source of the transit signal detected in the *K2* data.

For the close-in W–NW companion we cannot determine whether it is physically bound or unbound to K2-280. Yet, its very small angular separation of 0.4 arcsec supports the binary scenario for K2-280. Based on the `Besançon` Galactic population model[10] (Robin et al. 2003) and following the procedure described in Hjorth et al. (2019) we calculated the probability of a chance alignment to be 0.04 per cent. Assuming that the W–NW companion is physically bound to K2-280, we can then obtain further information about it.

The central wavelength of 2.19 µm of the Brγ filter is nearly identical to that of the near-infrared *K* band. Therefore we used the apparent *K* magnitude of K2-280 from Table 1 ($m_K = 10.765 \pm 0.019$) and the magnitude difference from Table 3 to calculate absolute *K* magnitudes of both stars. They are equal to $M_K = 2.778 \pm 0.090$ for K2-280 and $M_K = 7.50 \pm 0.22$ for the nearby companion. Making use of the Dartmouth isochrone table (Dotter et al. 2008) for metallicity [Fe/H] $= 0.36$ and ages between 9 and 11 Gyr, we estimated that the nearby companion is a M3.5–M4 red-dwarf with a mass between 0.21 and 0.28 ${\rm M}_\odot$. Using its angular separation from Table 3 and the DR2 parallax of K2-280 we calculated a lateral separation from K2-280 of $150.4^{+8.2}_{-7.7}$ au. We note that current models of planetary formations in wide binary stellar systems predict a shortage of giant planets in binaries with separations of $\lesssim$100 au (e.g. Nelson 2000; Mayer et al. 2005; Thébault, Marzari & Scholl 2006); the nearby companion should therefore not have affected the formation of the K2-280 planetary system.

Based on the Dartmouth isochrone table for metallicity [Fe/H] = 0.36 and ages between 9 and 11 Gyr, we also estimated the nearby star's absolute *Kepler* magnitude (M_{K_p}) as 10.75–11.5 mag, and its apparent *Kepler* magnitude as 18.75–19.5 mag. That is, its *Kepler* brightness is 0.0019 ± 50 per cent of K2-280's brightness. However, a false-positive scenario with an equal mass eclipsing binary (eclipse

[7] Available at http://stev.oapd.inaf.it/cgi-bin/param_1.3.

[8] We accounted for *Gaia* systematic uncertainties adding quadratically 0.1 mas to the nominal uncertainty of parallax (Luri et al. 2018).

[9] Available at https://idlastro.gsfc.nasa.gov/ftp/pro/astro/gal_uvw.pro.

[10] Available at http://modele2016.obs-besancon.fr.

Downloaded from https://academic.oup.com/mnras/article/497/4/4423/5873020 by University College London user on 25 September 2020

Table 4. K2-280 stellar and planetary parameters.

Parameter	Prior$^{(a)}$	Inferred value$^{(b)}$
Model parameters		
Orbital period $P_{\rm orb}$ (d)	$\mathcal{U}[19.89, 19.90]$	19.89526 ± 0.00028
Transit epoch T_0 (BJD$_{\rm TDB}$ −2450 000)	$\mathcal{U}[7307.55, 7307.65]$	7307.58114 ± 0.00056
Scaled semimajor axis $a/R_\star$	$\mathcal{N}[25.58, 0.90]$	$25.79^{+0.87}_{-0.90}$
Scaled planet radius $R_{\rm p}/R_\star$	$\mathcal{U}[0, 0.2]$	$0.05354^{+0.00094}_{-0.00056}$
Impact parameter, b	$\mathcal{U}[0, 1]$	$0.27^{+0.16}_{-0.17}$
$\sqrt{e}\sin\omega_\star$	$\mathcal{U}[-1, 1]$	$-0.547^{+0.047}_{-0.05}$
$\sqrt{e}\cos\omega_\star$	$\mathcal{U}[-1, 1]$	$-0.235^{+0.038}_{-0.043}$
Radial velocity semi-amplitude variation K (m s^{-1})	$\mathcal{U}[0, 50]$	9.18 ± 1.27
Parametrized limb-darkening coefficient q_1	$\mathcal{U}[0, 1]$	$0.54^{+0.14}_{-0.11}$
Parametrized limb-darkening coefficient q_2	$\mathcal{U}[0, 1]$	$0.249^{+0.082}_{-0.071}$
Systemic velocity $\gamma_{\rm HARPS\text{-}N}$ (km s^{-1})	$\mathcal{U}[-2.2, -0.2]$	$-1.1934^{+0.0011}_{-0.0011}$
Systemic velocity $\gamma_{\rm HARPS}$ (km s^{-1})	$\mathcal{U}[-2.2, -0.2]$	$-1.1907^{+0.0011}_{-0.0011}$
Systemic velocity $\gamma_{\rm FIES}$ (km s^{-1})	$\mathcal{U}[-2.2, -0.2]$	$-1.2349^{+0.0038}_{-0.0039}$
Jitter term $\sigma_{\rm HARPS\text{-}N}$ (m s^{-1})	$\mathcal{U}[0, 100]$	$0.36^{+0.97}_{-0.3}$
Jitter term $\sigma_{\rm HARPS}$ (m s^{-1})	$\mathcal{U}[0, 100]$	$1.28^{+1.76}_{-1.13}$
Jitter term $\sigma_{\rm FIES}$ (m s^{-1})	$\mathcal{U}[0, 100]$	$0.67^{+2.58}_{-0.58}$
Derived parameters planet b		
Planet mass $M_{\rm p}$ ($M_\oplus$)	···	37.1 ± 5.6
Planet radius $R_{\rm p}$ ($R_\oplus$)	···	7.50 ± 0.44
Planet density $\rho_{\rm p}$ (g cm^{-3})	···	$0.48^{+0.13}_{-0.10}$
Semimajor axis of the planetary orbit a (au)	···	$0.1461^{+0.0099}_{-0.0097}$
Orbital eccentricity, e	···	$0.35^{+0.05}_{-0.04}$
Inclination, i°	···	$89.53^{+0.30}_{-0.26}$
Angle of periastron, $\omega_\star$ (deg)	···	$246.77^{+4.54}_{-5.28}$
Time of periastron $T_{\rm p}$ (BJD$_{\rm TDB}$ −2450 000)	···	$7315.06^{+0.38}_{-0.44}$
Transit duration τ_{14} (h)	···	$8.267^{+0.063}_{-0.054}$
Equilibrium temperature$^{(c)}$ $T_{\rm eq}$ (K)	···	787 ± 17
Linear limb-darkening coefficient u_1	···	$0.367^{+0.074}_{-0.079}$
Quadratic limb-darkening coefficient u_2	···	$0.37^{+0.15}_{-0.15}$
Planet surface gravity$^{(d)}$ (cm s^{-2})	···	$648.0^{+107.0}_{-102.0}$
Planet surface gravity (cm s^{-2})	···	$647.0^{+133.0}_{-117.0}$

Notes. [a] $\mathcal{U}[a, b]$ refers to uniform priors between a and b, and $\mathcal{N}[a, b]$ to Gaussian priors with median a and standard deviation b.
[b] The inferred parameter value and its uncertainty are defined as the median and 68.3 percent credible interval of the posterior distribution.
[c] Assuming albedo =0.
[d] Calculated from the scaled-parameters as suggested by Southworth, Wheatley & Sams (2007).

depth equal to 50 per cent) and a transit signal with a depth of 3.5×10^{-3} can only be caused by a binary that is brighter than 0.007 times the host's brightness. Therefore, assuming that the nearby W–NW star is physically bound with K2-280, we may exclude it as a source of a false positive.

4 GLOBAL ANALYSIS

We used the code `pyaneti` (Barragán, Gandolfi & Antoniciello 2019) to perform the joint analysis of the RV and *K2* transit data. The code uses the limb-darkened quadratic model by Mandel & Agol (2002) to fit the transit light curves and a Keplerian model for the RV measurements. We integrated the light-curve model over 10 steps to simulate the *Kepler* long-cadence integration (Kipping 2010). Fitted parameters, parametrizations, and likelihood are similar to previous analysis performed with `pyaneti` (e.g. Barragán et al. 2016, 2018a).

The photometric data include ∼17 h (i.e. twice the transit duration) of data points centred around each of the 4 transits observed by *K2*. We de-trended the photometric chunks using the program `exotrending` (Barragán & Gandolfi 2017). Fitting a second-order polynomial to the out-of-transit data. The Doppler measurements include the 6 FIES, 14 HARPS-N, and 18 HARPS RVs presented in Section 2.2.

We adopted uniform priors for all the parameters; details are given in Table 4. We started 500 Markov chains randomly distributed inside the prior ranges. Once all chains converged,[11] we ran 5000 additional iterations. We used a thin factor of 10 to generate a posterior distribution of 250 000 independent points for each parameter.

[11] We define convergence as when chains have a scaled potential factor <1.02 for all the parameters (see Gelman & Rubin 1992, for more details).

Downloaded from https://academic.oup.com/mnras/article/497/4/4423/5873020 by University College London user on 25 September 2020

Table 5. Model comparison for our RV fits.

Test	Npars	Log likelihood	BIC	K($\mathrm{m\,s^{-1}}$)
No planet – no jitter	3	118	−226	0
No planet – jitter	6	135	−248	0
Planet – circular orbit – no jitter	6	136	−249	7.20 ± 1.15
Planet – circular orbit – jitter	9	143	−254	7.18 ± 1.60
Planet – eccentric orbit – no jitter	8	154	−280	9.31 ± 1.20
Planet – eccentric orbit – jitter	11	154	−269	9.27 ± 1.30

Note. Further details about the Bayesian Information Criterion (BIC) are given in, e.g. Burnham & Anderson (2002).

We first explored the properties of the Doppler signal by fitting the RV data alone. We tested different models: one model assumes there is no Doppler reflex motion; one model assumes the presence of a planet on a circular orbit; another model assumes the presence of a planet on an eccentric orbit. These three models were run with and without a jitter term for each instrument. This generates a set of six different models. The main statistical properties of each model are listed in Table 5. From this Table we can draw the following conclusions: (1) the models including a planet signal are strongly preferred over the models without it; (2) the eccentric model is preferred, as suggested also by the transit fit (see the following paragraph); (3) the model does not require to add a jitter term for each spectrograph, suggesting that any extra signal (stellar variability, other planets, etc.) are below the instrumental precision. This supports our RV analysis assuming only a Keplerian orbit. We note that we still fit for a jitter term for each instrument to allow more flexibility to our modelling and to mitigate the effects of the relatively sparse sampling of our data on the accuracy of the semi-amplitude estimate.

We used Kepler's third law to check if the stellar density derived from the modelling of the transit light curves is consistent with an eccentric orbit (see e.g. Van Eylen & Albrecht 2015). We first ran an MCMC analysis assuming the orbit is circular. The derived stellar density is $0.32^{+0.02}_{-0.06}\,\mathrm{g\,cm^{-3}}$. This density disagrees with the stellar density of $0.8^{+0.16}_{-0.13}\,\mathrm{g\,cm^{-3}}$ obtained from the spectroscopic parameters derived in Section 3. We then performed a joint analysis allowing for an eccentric solution. We derived a stellar density of $0.82^{+0.38}_{-0.35}\,\mathrm{g\,cm^{-3}}$, which is consistent with the spectroscopically derived stellar density. This provides further evidence that the planetary orbit is eccentric. For the final analysis, we decided to set a Gaussian prior on $a/R_\star$ using Kepler's third law and the stellar mass and radius derived in Section 3 and listed in Table 1.

The median and 68.3 per cent percent credible intervals of the marginalized posterior distributions are reported in Table 4. Fig. 4 displays the RV and transit data together with the best-fitting model. We show a corner plot of the fitted parameters in Fig. A1.

The HARPS, HARPS-N, and FIES Doppler measurements show an RV variation in phase with the transit ephemeris (Fig. 4, lower panel). However, as described by Cunha et al. (2013), contaminant stars that are within the sky-projected angular size of the spectrograph fibre (1 arcsec for HARPS and HARPS-N, 1.3 arcsec for FIES) may affect the radial velocity measurements of the target star. If the radial velocity of the contaminant star is changing, i.e. its spectrum is shifting across the spectrum of target star, it can distort the spectral line profile of the target (and hence its CCF), mimicking the presence of an orbiting planet. As presented by Cunha et al. (2013) in their table 8, for magnitude differences of ∼5–6 mag, the impact of F2 V–K5 V contaminant star on a G8 V target star can be as high as $10\,\mathrm{m\,s^{-1}}$. If the nearby N–NW star, which has an angular separation 0.38 ± 0.011 arcsec from K2-280, is an F or G background eclipsing binary, it may not only generate a transit-like signal in the light curve of K2-280 every 19.9 d, but also a low-amplitude radial velocity signal at this period. We carefully checked the FWHM and BIS of the HARPS, HARPS-N, and FIES CCFs to search for potential line profile variation induced by the blend companion. The generalized Lomb–Scargle periodograms (Zechmeister & Kürster 2009) of these indicators show no significant signal neither at the 19.9-d period and its harmonics, nor at any other period. We also found no correlation between the FWHM and BIS, and the RV measurements (Fig. 5). In particular, the Spearman correlation coefficient between the HARPS RV measurements and the BIS of CCFs is equal to $r_{\mathrm{RV-BIS,\,HARPS}} = -0.45$ and between HARPS RVs and FWHM is equal to $r_{\mathrm{RV-FWHM,\,HARPS}} = -0.18$. The Spearman correlation coefficient between the HARPS-N RVs and

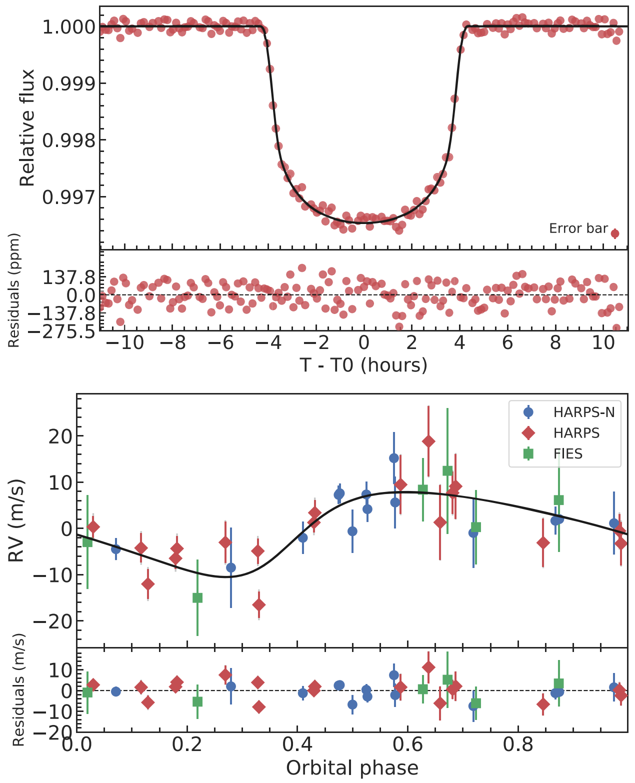

Figure 4. Top panel: Transit light curve folded to the orbital period of K2-280 b and residuals. The thick black line is the re-binned best-fitting transit model. The red points are the *K2* data. Bottom panel: The RV curve of K2-280 b phase-folded to the orbital period of the planet. The best-fitting solution is marked with a solid black line. HARPS-N, HARPS, and FIES data are shown with blue circles, red diamonds, and green squares, respectively. The lower panel shows the residuals to the best-fitting model.

Downloaded from https://academic.oup.com/mnras/article/497/4/4423/5873020 by University College London user on 25 September 2020

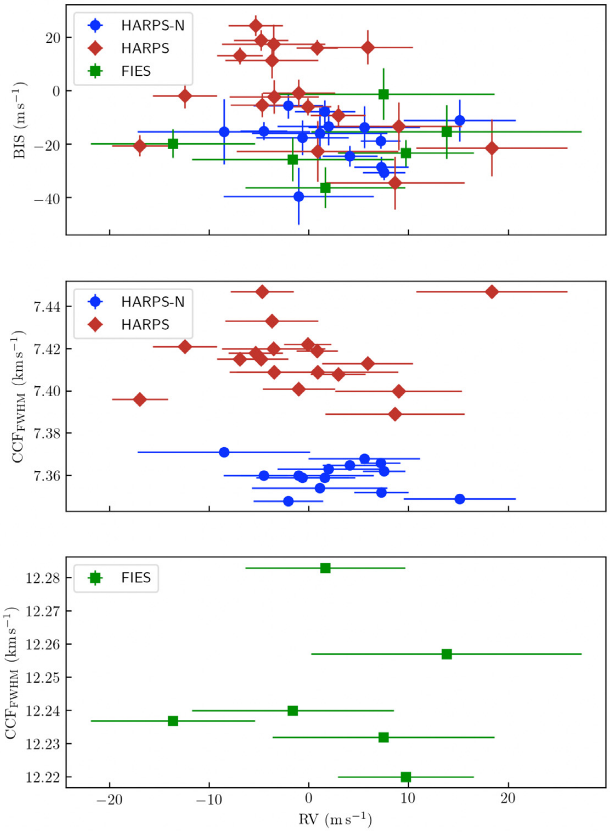

Figure 5. Top panel: The BIS versus RVs from HARPS-N, HARPS, and FIES. Middle panel: The CCF_{FWHM} versus RVs from HARPS-N and HARPS. Bottom panel: The CCF_{FWHM} versus RVs from FIES. RVs from all instruments have been subtracted by the systemic velocities listed in Table 4 and derived by our joint analysis.

BIS is equal to $r_{\mathrm{RV-BIS,\,HARPS\text{-}N}} = -0.19$ and between the HARPS-N RVs and FWHM is equal to $r_{\mathrm{RV-FWHM,\,HARPS\text{-}N}} = -0.06$. In the case of FIES measurements, the Spearman correlation coefficient between RVs and BIS is equal to $r_{\mathrm{RV-BIS,\,FIES}} = 0.37$ and between RVs and FWHM is equal to $r_{\mathrm{RV-FWHM,\,FIES}} = -0.08$.

We note that we could not measure the stellar rotation period from the *K2* light curve. Using the stellar radius determined in Section 3.4 and the projected rotation velocity determined in Section 3.2, we found the upper limit of the stellar rotation period to be $P_{\mathrm{rot}} = 21.6^{+12.6}_{-6.3}$ d. This means that the stellar rotation period of K2-280 is shorter than 34.2 d. Following the prescription given by Aigrain, Pont & Zucker (2012), the photometric variation found in the *K2* light curve (∼600 ppm) implies an activity induced RV signal of about 2 m s^{-1} (1.9 m s^{-1} for stellar rotation period equal to orbital period of K2-280 b (19.9 d) or 1.1 m s^{-1} for P_{rot} equal to 34.2 d). The probability that stellar rotation modulation may generate RV variations of K2-280 is therefore very low. We conclude that most likely the Doppler shift of K2-280 is induced by the orbital motion of a planet transiting K2-280 rather than a blended eclipsing binary or stellar rotation modulation. We stress however that the activity-induced RV signal at a level of ∼2 m s^{-1} is larger than the jitter terms listed in Table 4 and larger than the precision on our estimate of the Doppler semi-amplitude variation induced by the planet ($K = 9.18 \pm 1.27$ m s^{-1}). Therefore, we warn the reader that our semi-amplitude estimate might be affected by unaccounted for stellar activity.

5 DISCUSSION AND SUMMARY

5.1 K2-280 b and the current sample of sub-Saturn planets

With a mass of $M_{\mathrm{b}} = 37.1 \pm 5.6$ $\mathrm{M}_{\oplus}$ and a radius of $R_{\mathrm{b}} = 7.50 \pm 0.44$ $\mathrm{R}_{\oplus}$, K2-280 b joins the group of sub-Saturns planets – defined as planets having radii between 4 and 8 $\mathrm{R}_{\oplus}$ (Petigura et al. 2017) – whose masses and radii have been measured. The basic physical parameters of a sample of 23 sub-Saturns with densities measured with a precision better than 50 per cent have been presented and discussed by Petigura et al. (2017). We here extend this sample by adding K2-280 b alongside 6 additional sub-Saturns that have densities measured with a precision better than 50 per cent, as described below. WASP-156 b (Demangeon et al. 2018), an ∼0.5 $\mathrm{R}_{\mathrm{Jup}}$ planet with a Jupiter-like density was discovered by the ground-based SuperWASP transit survey (Pollacco et al. 2006; Smith & WASP Consortium 2014). Kepler-1656 b, a dense sub-Saturn with a high eccentricity of $e = 0.84$ transiting a relatively bright ($V = 11.6$ mag) solar-type star, was recently reported by Brady et al. (2018). Three sub-Saturns were discovered and characterized by the KESPRINT consortium, two of them in *K2* campaign 3 (K2-60 b, Eigmüller et al. 2017) and campaign 14 (HD 89345 b, aka K2-234 b, Van Eylen et al. 2018; Yu et al. 2018b), and HD 219666 b (Esposito et al. 2019) in *TESS* Sector 1. One sub-Saturn, GJ 3470 b (Bonfils et al. 2012), orbiting an M1.5 dwarf was not included by Petigura et al. (2017), but we add it to the current sample, adopting the parameters from Awiphan et al. (2016). All of these new sub-Saturns, including K2-280 b, reside in apparently single systems. Fig. 6 shows the mass–radius and mass–density diagrams for this extended sample of 30 planets. Sub-Saturns found to be in multiplanet systems are marked with green filled circles, whereas those in single systems are marked with blue filled circles. The position of K2-280 b is indicated with a red-rimmed circle. Sub-Saturns whose density has been measured with a precision slightly worse than 50 per cent are marked with green and blue open circles. All the remaining transiting planets with measured radii and masses are marked with open grey circles.[12] According to the Fortney, Marley & Barnes (2007)'s models – also shown in the mass–radius diagram (Fig. 6, upper panel) – K2-280 b has a core of about 10–25 $\mathrm{M}_{\oplus}$, accounting for ∼25–65 per cent of its total mass.

The diagrams in Fig. 6 confirm the main characteristics found by Petigura et al. (2017) for the population of sub-Saturns. One of the main property is the uniform distribution of masses in the range ∼5–75 $\mathrm{M}_{\oplus}$. With a mass of 135 ± 12 $\mathrm{M}_{\oplus}$ and radius of 7.66 ± 0.41 $\mathrm{R}_{\oplus}$, K2-60 b (Eigmüller et al. 2017) is close to the lower envelope of giant planets on the mass–radius diagram and is the only sub-Saturn-sized planet with a mass higher than Saturn (95.16 $\mathrm{M}_{\oplus}$). With a mean density of 1.7 ± 0.3 g cm^{-3} (i.e. Neptune's density), K2-60 b is also the most dense planet in the mass range ∼75–250 $\mathrm{M}_{\oplus}$. As stressed by Eigmüller et al. (2017), K2-60 b with radius smaller than expected from the models of Laughlin, Crismani & Adams (2011) is more dense than expected and close to the sub-Jovian desert characterized by scarcity of planets with orbital periods below 4 d and masses lower than ∼300 $\mathrm{R}_{\oplus}$ (Szabó & Kiss 2011; Beaugé & Nesvorný 2013; Mazeh, Holczer & Faigler 2016). The underestimation of its radius was excluded based on AO imaging (Schmitt et al. 2016). Only radial accelerations lower than 2 m s^{-1} d^{-1} that cannot be excluded based on RVs collected by Eigmüller et al. (2017) suggest that mass of

[12] As retrieved from the NASA Exoplanet Archive (Akeson et al. 2013) – 2019 July.

Downloaded from https://academic.oup.com/mnras/article/497/4/4423/5873020 by University College London user on 25 September 2020

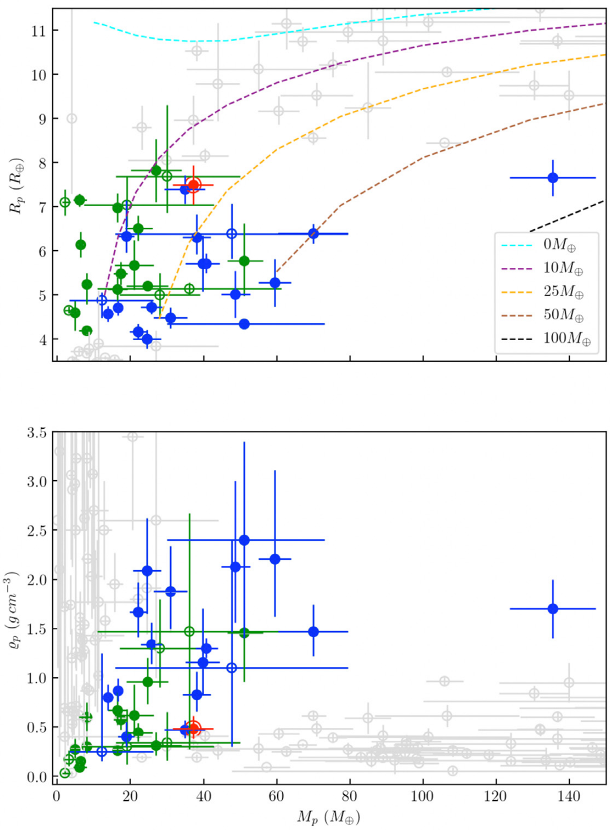

Figure 6. Mass–radius (upper panel) and mass–density (lower panel) diagrams for a sample of sub-Saturns (R_p = 4–8 $R_\oplus$). Sub-Saturns whose mean densities have been measured with a precision better than 50 per cent located in multiplanet systems are marked with green filled circles, whereas those in single systems are marked with blue filled circles. The position of K2-280 b is indicated as a red-rimmed circle. Sub-Saturns with densities measured with a precision slightly worse than 50 per cent are marked with green and blue open circles. The remaining planets with measured radii, masses, and mean densities (NASA Exoplanet Archive (Akeson et al. 2013), as of 2019 July] are marked with open grey circles. The dashed lines on the mass–radius diagram (upper panel) correspond to the Fortney et al. (2007) models for planet core masses of 0, 10, 25, 50, and 100 $M_\oplus$ and age 10 Gyr.

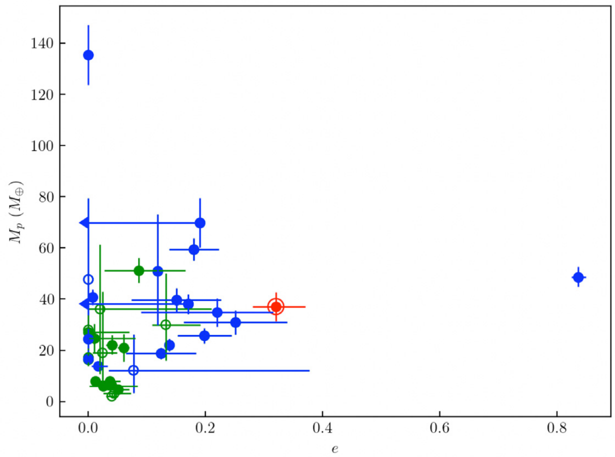

Figure 7. Mass of sub-Saturn planets as a function of the eccentricity. Samples and point symbols as in Fig. 6.

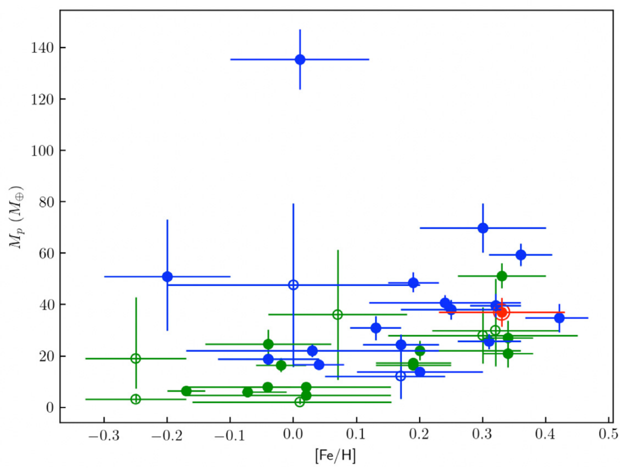

Figure 8. Mass of sub-Saturn planets as a function of iron content of their host stars. Samples and point symbols as in Fig. 6.

K2-60 b may be lower than current determination. Nevertheless, this intriguing planet may help with a study of sub-Jovian desert and its borders.

Although the mass distribution of sub-Saturns is quite uniform, the most massive ones have radii close to and below ∼6 $R_\oplus$, visible as a correlation on the mass–density diagram (Fig. 6, lower panel). The Spearman correlation coefficient between mass and density for the current sample of 30 sub-Saturns (excluding K2-60 b) is equal to r = 0.72. This correlation is comparable to the one for the sample of 23 planets discussed in Petigura et al. (2017) that is equal to r = 0.79. Notably, almost all of the most massive sub-Saturns from the current sample of 30 planets reside in apparently single-planet systems (blue circles in Fig. 6). Sub-Saturns in single-planet systems have also often moderate eccentricities, higher than their counterparts in multiplanet systems, as shown in Fig. 7. As suggested by Petigura et al. (2017), the moderate eccentricities of more massive sub-Saturns in apparently single systems and the lack of high-eccentricity, high-mass objects in multi-planet systems may be explained by scattering and merging events during the formation process.

Petigura et al. (2017) found a marginal correlation between the stellar metallicity and the mass of sub-Saturn planets (the Spearman correlation coefficient $r = 0.57$), with the massive sub-Saturns found to orbit metal-rich stars. We confirm this for the current sample of 30 sub-Saturns (excluding K2-60 b) with exactly the same value of the Spearman correlation coefficient. This is consistent with the results of Buchhave et al. (2012) who, based on the sample of Kepler planets, found that planets larger than ∼4 $R_\oplus$ orbit stars with relatively high metal content (−0.2 < [Fe/H] < 0.5 dex). For the sake of consistency with Figs 6 and 7, we included in Fig. 8 the sub-Saturns orbiting binary stars, namely, Kepler-47 (AB) c and d ([Fe/H] = −0.25 ± 0.08 dex) and Kepler-413 (AB) b ([Fe/H] = −0.2 ± 0.1 dex), which were omitted by Petigura et al. (2017). Given its mass of M_p = 37.1 ± 5.6 $M_\oplus$ and the iron content of its host star ([Fe/H] = 0.33 ± 0.08 dex), K2-280 b follows this trend, being a relatively massive sub-Saturn orbiting a metal rich star.

K2-280 b has a relatively long orbital period of ∼19.9 d and transits a slightly evolved star in an apparently single-planet system. With an eccentricity of $e = 0.35^{+0.05}_{-0.04}$, K2-280 b is exactly within the

Downloaded from https://academic.oup.com/mnras/article/497/4/4423/5873020 by University College London user on 25 September 2020

range of eccentricities found by Van Eylen et al. (2019) for *Kepler* systems with single transiting giant planets ($R_p > 6\,R_\oplus$). After Kepler-1656 b (Brady et al. 2018), K2-280 b is the second most eccentric sub-Saturn known to date. In contrast to Kepler-1656 b, the mass of $M_b = 37.1 \pm 5.6$ M$_\oplus$, radius of $R_b = 7.50 \pm 0.44$ R$_\oplus$, and mean density of $\rho_b = 0.48^{+0.13}_{-0.10}$ g cm^{-3}, make K2-280 b more similar to HD 89345 b (aka K2-234 b; Van Eylen et al. 2018; Yu et al. 2018b). The moderate eccentricity of K2-280 b suggests a formation pathway involving planet–planet gravitational interactions, and make this sub-Saturn planet a member of a relatively rare group of exoplanets and an interesting object for possible future follow-up.

5.2 Prospects for atmospheric characterization and Rossiter–McLaughlin effect measurements

Although K2-280 b is a quite puffy planet, the relatively large radius of its host star ($R_\star = 1.28 \pm 0.07$ R$_\odot$) results in a quite low transmission signal per scale height (H) of the planetary atmosphere (55 ppm). This makes it a difficult target for atmospheric characterization with current ground- and space-based facilities. The transmission spectroscopy metric (TSM) defined by Kempton et al. (2018) for JWST/NIRISS is ~45 for K2-280 b, i.e. two times lower than the threshold TSM for planets with radii $R_p \in (1.5 - 10.0)\,R_\oplus$ to be selected as high-quality atmospheric characterization targets. The long transit duration (~8 h) further complicates ground-based follow-up observations.

Still, there is a possibility of Rossiter–McLaughlin (RM) effect measurements, for which the overall amplitude is expected to be ~6 m s^{-1}, depending on the real values of stellar projected rotation velocity and planetary and stellar radii. With an impact parameter of $b = 0.27^{+0.16}_{-0.17}$, the transit of K2-280 b is close to being central. In such a case the shape of the RM effect would not change significantly with the sky-projected spin-orbit angle λ, but mainly the RM amplitude, leading to a strong correlation between λ and $v_{\rm rot} \sin i_\star$ (see e.g. Albrecht et al. 2011). Therefore more precise determination of $v_{\rm rot} \sin i_\star$ of this slow rotator, based for instance on the Fourier transform technique (e.g. Smith & Gray 1976; Dravins, Lindegren & Torkelsson 1990; Gray 2008, and references therein) applied to single very high resolution and high SNR line profiles, would be needed. Measurements of the sky-projected spin-orbit angle through RM observations may help to test formation scenarios of warm sub-Saturn planets. This gives additional arguments for attempting RM observations, as the probability of a misalignment between the planet's orbital angular momentum vector and its host star's spin axis should be higher if caused by a perturber than by primordial misalignment of the protoplanetary disc. Two full transits of K2-280 b observable from the Chilean observatories will occur on 2020 July 7th/8th and 2021 August 9th/10th.

6 CONCLUSIONS

We report here detailed characterization of a low-density ($\rho_b = 0.48^{+0.13}_{-0.10}$ g cm^{-3}) sub-Saturn transiting a mildly evolved, metal rich G7 star K2-280. With a mass of $M_b = 37.1 \pm 5.6$ M$_\oplus$, a radius of $R_b = 7.50 \pm 0.44$ R$_\oplus$, and an eccentricity of $e = 0.35^{+0.05}_{-0.04}$, K2-280 b joins the group of sub-Saturns planets in apparently single-planet systems. This second most eccentric sub-Saturn known to date is an interesting object for possible future follow-up observations that may help to test formation scenarios of this intriguing group of planets that are absent in the Solar system.

ACKNOWLEDGEMENTS

This work was supported by the Spanish Ministry of Economy and Competitiveness (MINECO) through grants ESP2016-80435-C2-1-R and ESP2016-80435-C2-2-R. SM acknowledges support from the Spanish Ministry with the Ramon y Cajal fellowship number RYC-2015-17697. This is University of Texas Center for Planetary Systems Habitability contribution #0010. OB acknowledges support from the UK Science and Technology Facilities Council (STFC) under grants ST/S000488/1 and ST/R004846/1. CMP, MF, and IG gratefully acknowledge the support of the Swedish National Space Agency (DNR 163/16 and 174/18). JK, SG, MP, SC, APH, and HR acknowledge support by Deutsche Forschungsgemeinschaft (DFG) grants PA525/18-1, PA525/19-1, PA525/20-1, HA 3279/12-1, and RA 714/14-1 within the DFG Schwerpunkt SPP 1992, Exploring the Diversity of Extra-solar Planets. This work is partly supported by JSPS KAKENHI Grant Numbers JP18H01265, JP18H05439, and JP16K17660, and JST PRESTO Grant Number JPMJPR1775. RB acknowledges support from FONDECYT Postdoctoral Fellowship Project 3180246. AJ acknowledges support from FONDECYT project 1171208. RB, AJ, and FR acknowledge additional support from the Ministry for the Economy, Development, and Tourism's Programa Iniciativa Científica Milenio through grant IC 120009, awarded to the Millennium Institute of Astrophysics (MAS).

We are very grateful to the Gemini-North, NOT, HARPS, and HARPS-N staff members for their unique support during the observations. Based on observations obtained at the Gemini Observatory, which is operated by the Association of Universities for Research in Astronomy, Inc., under a cooperative agreement with the NSF on behalf of the Gemini partnership: the National Science Foundation (United States), National Research Council (Canada), CONICYT (Chile), Ministerio de Ciencia, Tecnología e Innovación Productiva (Argentina), Ministério da Ciência, Tecnologia e Inovação (Brazil), and Korea Astronomy and Space Science Institute (Republic of Korea). Based on observations obtained with the Nordic Optical Telescope (NOT), operated on the island of La Palma jointly by Denmark, Finland, Iceland, Norway, and Sweden, in the Spanish Observatorio del Roque de los Muchachos (ORM) of the Instituto de Astrofísica de Canarias (IAC) under programme 53-109. Based on observations collected at the European Organisation for Astronomical Research in the Southern Hemisphere under ESO programmes 097.C-0571(B), 097.C-0948(A), 098.C-0860(A), 099.C-0491(A), 0101.C-0407(A), and 60.A-9700(G). Based on observations made with the Italian Telescopio Nazionale Galileo (TNG) operated on the island of La Palma by the Fundación Galileo Galilei of the INAF (Istituto Nazionale di Astrofisica) at the Spanish Observatorio del Roque de los Muchachos of the Instituto de Astrofisica de Canarias under programmes A33TAC_15, OPT17A_64, CAT17A_91, and CAT19A_97.

This paper includes data collected by the Kepler mission. Funding for the Kepler mission is provided by the NASA Science Mission directorate. This work has made use of data from the European Space Agency (ESA) mission *Gaia* (https://www.cosmos.esa.int/gaia), processed by the *Gaia* Data Processing and Analysis Consortium (DPAC, https://www.cosmos.esa.int/web/gaia/dpac/consortium). Funding for the DPAC has been provided by national institutions, in particular the institutions participating in the *Gaia* Multilateral Agreement. This research has made use of NASA Exoplanet Archive and NASA's Astrophysics Data System.

Facility: *Kepler*, *Gaia*, Gemini-North/NIRI+ALTAIR, ESO/HARPS, TNG/HARPS-N, NOT/FIES.

Software: `BLS`, `IRAF`, `PARAM 1.3`, `pyaneti`, `SME`, `SpecMatch-emp`.

Downloaded from https://academic.oup.com/mnras/article/497/4/4423/5873020 by University College London user on 25 September 2020

DATA AVAILABILITY

The data underlying this article are available in the article and in its online supplementary material.

REFERENCES

Aigrain S., Pont F., Zucker S., 2012, MNRAS, 419, 3147
Akeson R. L. et al., 2013, PASP, 125, 989
Albrecht S. et al., 2011, ApJ, 738, 50
Awiphan S. et al., 2016, MNRAS, 463, 2574
Bailer-Jones C. A. L., Rybizki J., Fouesneau M., Mantelet G., Andrae R., 2018, AJ, 156, 58
Baranne A. et al., 1996, A&AS, 119, 373
Barragán O., Gandolfi D., 2017, Astrophysics Source Code Library, record ascl:1706.001
Barragán O. et al., 2016, AJ, 152, 193
Barragán O. et al., 2018a, MNRAS, 475, 1765
Barragán O. et al., 2018b, A&A, 612, A95
Barragán O., Gandolfi D., Antoniciello G., 2019, MNRAS, 482, 1017
Beaugé C., Nesvorný D., 2013, ApJ, 763, 12
Bonfils X. et al., 2012, A&A, 546, A27
Borucki W. J. et al., 2010, Science, 327, 977
Brady M. T. et al., 2018, AJ, 156, 147
Bressan A., Marigo P., Girardi L., Salasnich B., Dal Cero C., Rubele S., Nanni A., 2012, MNRAS, 427, 127
Bruntt H. et al., 2010, MNRAS, 405, 1907
Buchhave L. A. et al., 2010, ApJ, 720, 1118
Buchhave L. A. et al., 2012, Nature, 486, 375
Burnham K., Anderson D., 2002, Model Selection and Multimodel Inference: A Practical Information-Theoretic Approach. Springer-Verlag, New York
Christiansen J. L. et al., 2017, AJ, 154, 122
Cosentino R. et al., 2012, McLean I. S., Ramsay S. K., Hideki T., Proc. SPIE Conf. Ser. Vol. 8446, Ground-based and Airborne Instrumentation for Astronomy IV. SPIE, Belligham, p. 84461V
Coşkunoğlu B. et al., 2011, MNRAS, 412, 1237
Crossfield I. J. M. et al., 2016, ApJS, 226, 7
Crossfield I. J. M. et al., 2018, ApJS, 239, 5
Cunha D., Figueira P., Santos N. C., Lovis C., Boué G., 2013, A&A, 550, A75
Dai F., Winn J. N., Yu L., Albrecht S., 2017, AJ, 153, 40
Demangeon O. D. S. et al., 2018, A&A, 610, A63
Dorn C., Khan A., Heng K., Connolly J. A. D., Alibert Y., Benz W., Tackley P., 2015, A&A, 577, A83
Dotter A., Chaboyer B., Jevremović D., Kostov V., Baron E., Ferguson J. W., 2008, ApJS, 178, 89
Doyle A. P., Davies G. R., Smalley B., Chaplin W. J., Elsworth Y., 2014, MNRAS, 444, 3592
Dravins D., Lindegren L., Torkelsson U., 1990, A&A, 237, 137
Dressing C. D. et al., 2017, AJ, 154, 207
Eastman J., Siverd R., Gaudi B. S., 2010, PASP, 122, 935
Eigmüller P. et al., 2017, AJ, 153, 130
Esposito M. et al., 2019, A&A, 623, A165
Foreman-Mackey D., 2016, J. Open Source Softw., 1, 24
Fortney J. J., Marley M. S., Barnes J. W., 2007, ApJ, 659, 1661
Frandsen S., Lindberg B., 1999, in Karttunen H., Piirola V., eds, Proc. Conf. Astrophysics with the NOT. Univ. Turku, Tuorla Observatory, Finland, p. 71
Fridlund M. et al., 2017, A&A, 604, A16
Gaia Collaboration, 2016, A&A, 595, A1
Gaia Collaboration, 2018, A&A, 616, A1
Gandolfi D. et al., 2008, ApJ, 687, 1303
Gandolfi D. et al., 2015, A&A, 576, A11
Gandolfi D. et al., 2017, AJ, 154, 123
Gelman A., Rubin D. B., 1992, Stat. Sci., 7, 457
Gray D. F., 2008, The Observation and Analysis of Stellar Photospheres. Cambridge Univ. Press, Cambridge, UK
Gray R. O., Corbally J. C., 2009, Stellar Spectral Classification. Princeton University Press, NJ
Hekker S., Reffert S., Quirrenbach A., Mitchell D. S., Fischer D. A., Marcy G. W., Butler R. P., 2006, A&A, 454, 943
Hekker S., Snellen I. A. G., Aerts C., Quirrenbach A., Reffert S., Mitchell D. S., 2008, A&A, 480, 215
Hirano T. et al., 2018, AJ, 155, 127
Hjorth M. et al., 2019, MNRAS, 484, 3522
Hodapp K. W. et al., 2003, PASP, 115, 1388
Howell S. B. et al., 2014, PASP, 126, 398
Jenkins J. M. et al., 2010, ApJ, 713, L87
Johnson D. R. H., Soderblom D. R., 1987, AJ, 93, 864
Kempton E. M. R. et al., 2018, PASP, 130, 114401
Kipping D. M., 2010, MNRAS, 408, 1758
Kovács G., Zucker S., Mazeh T., 2002, A&A, 391, 369
Kurucz R. L., 2013, Astrophysics Source Code Library, record ascl:1303.024
Laughlin G., Crismani M., Adams F. C., 2011, ApJ, 729, L7
Livingston J. H. et al., 2018, AJ, 156, 277
Luri X. et al., 2018, A&A, 616, A9
Malavolta L. et al., 2018, AJ, 155, 107
Mandel K., Agol E., 2002, ApJ, 580, L171
Mayer L., Wadsley J., Quinn T., Stadel J., 2005, MNRAS, 363, 641
Mayo A. W. et al., 2018, AJ, 155, 136
Mayor M. et al., 2003, The Messenger, 114, 20
Mazeh T., Holczer T., Faigler S., 2016, A&A, 589, A75
Montet B. T. et al., 2015, ApJ, 809, 25
Nelson A. F., 2000, ApJ, 537, L65
Ofir A., 2014, A&A, 561, A138
Pepe F. et al., 2013, Nature, 503, 377
Persson C. M. et al., 2018, A&A, 618, A33
Petigura E. A. et al., 2016, ApJ, 818, 36
Petigura E. A. et al., 2017, AJ, 153, 142
Petigura E. A. et al., 2018, AJ, 155, 21
Piskunov N., Valenti J. A., 2017, A&A, 597, A16
Pollacco D. L. et al., 2006, PASP, 118, 1407
Prieto-Arranz J. et al., 2018, A&A, 618, A116
Reddy B. E., Lambert D. L., Allende Prieto C., 2006, MNRAS, 367, 1329
Robin A. C., Reylé C., Derrière S., Picaud S., 2003, A&A, 409, 523
Rodriguez J. E., Vanderburg A., Eastman J. D., Mann A. W., Crossfield I. J. M., Ciardi D. R., Latham D. W., Quinn S. N., 2018, AJ, 155, 72
Schmitt J. R. et al., 2016, AJ, 151, 159
Smith M. A., Gray D. F., 1976, PASP, 88, 809
Smith A. M. S., WASP Consortium, 2014, Contributions of the Astronomical Observatory Skalnaté Pleso, 43, 500
Southworth J., Wheatley P. J., Sams G., 2007, MNRAS, 379, L11
Szabó G. M., Kiss L. L., 2011, ApJ, 727, L44
Tayar J., Stassun K. G., Corsaro E., 2019, ApJ, 883, 195
Telting J. H. et al., 2014, Astron. Nachr., 335, 41
Thébault P., Marzari F., Scholl H., 2006, Icarus, 183, 193
Torres G., Andersen J., Giménez A., 2010, A&AR, 18, 67
Udry S., Mayor M., Queloz D., 1999, in Hearnshaw J. B., Scarfe C. D., eds, ASP Conf. Ser. Vol. 185, IAU Colloq. 170: Precise Stellar Radial Velocities. Astron. Soc. Pac., San Francisco, p. 367
Valenti J. A., Fischer D. A., 2005, ApJS, 159, 141
Valenti J. A., Piskunov N., 1996, A&AS, 118, 595
Van Eylen V. et al., 2018, MNRAS, 478, 4866
Van Eylen V. et al., 2019, AJ, 157, 61
Van Eylen V., Albrecht S., 2015, ApJ, 808, 126
Vanderburg A. et al., 2015, ApJ, 800, 59
Vanderburg A. et al., 2016, ApJS, 222, 14
Vogt S. S. et al., 1994, in Crawford D. L., Craine E. R., eds, Proc. SPIE Conf. Ser. Vol. 2198, Instrumentation in Astronomy VIII. SPIE, Belligham, p. 362
Winn J. N., Sanchis-Ojeda R., Rappaport S., 2018, New Astron. Rev., 83, 37
Yee S. W., Petigura E. A., von Braun K., 2017, ApJ, 836, 77
Yu L. et al., 2018a, AJ, 156, 22
Yu L. et al., 2018b, AJ, 156, 127
Zechmeister M., Kürster M., 2009, A&A, 496, 577

Downloaded from https://academic.oup.com/mnras/article/497/4/4423/5873020 by University College London user on 25 September 2020

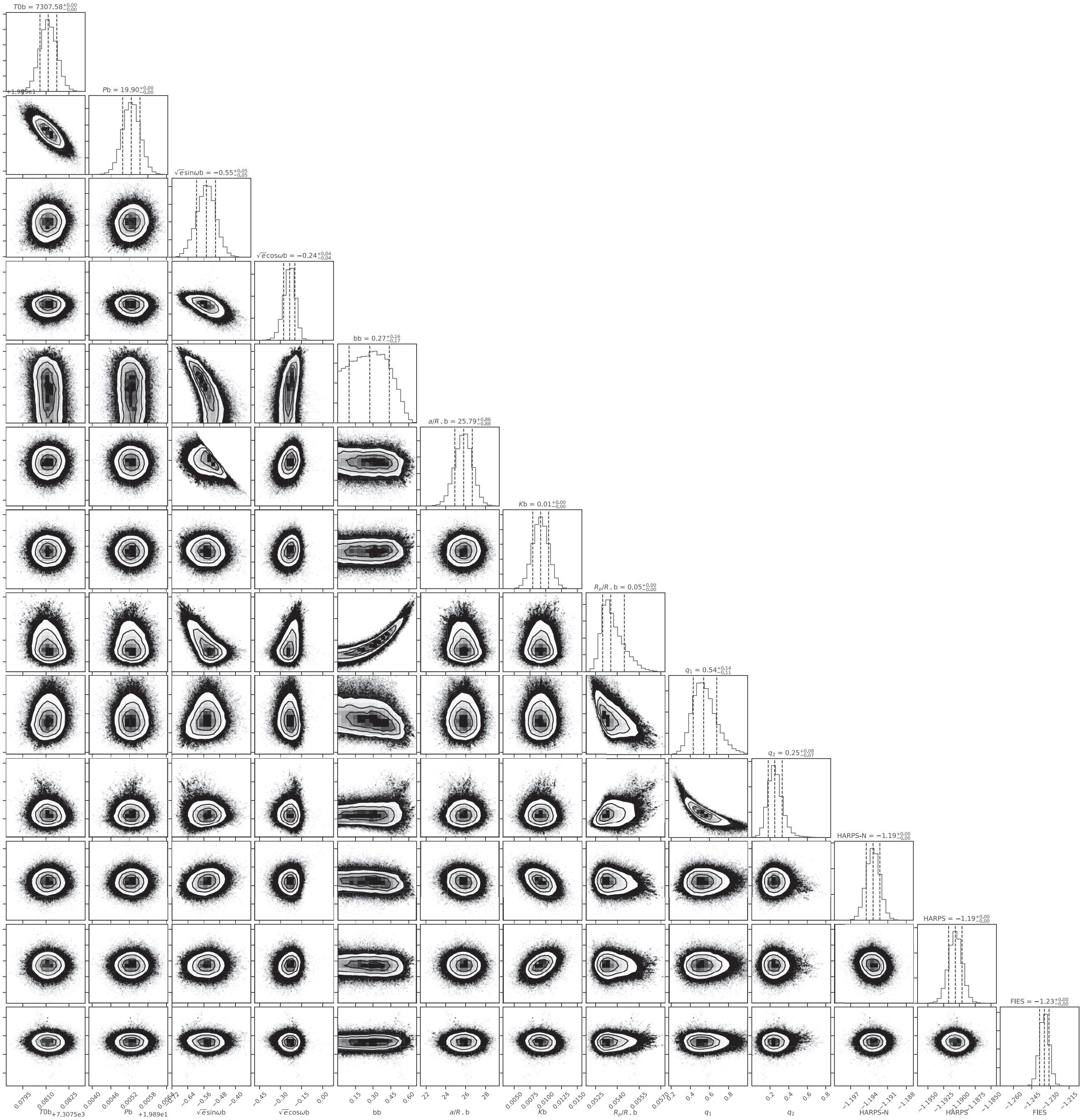

Figure A1. Corner plot for the fitted parameters of the K2-280 system. This figure was created using `corner.py` (Foreman-Mackey 2016).

APPENDIX: CORNER PLOT FOR FITTED PARAMETERS

[1] *Instituto de Astrofísica de Canarias (IAC), E-38205 La Laguna, Tenerife, Spain*
[2] *Departamento de Astrofísica, Universidad de La Laguna (ULL), E-38206 La Laguna, Tenerife, Spain*
[3] *Dipartimento di Fisica, Universitá di Torino, Via P. Giuria 1, I-10125, Torino, Italy*
[4] *Department of Earth and Planetary Sciences, Tokyo Institute of Technology, 2-12-1 Ookayama, Meguro-ku, Tokyo, Japan*
[5] *Sub-department of Astrophysics, Department of Physics, University of Oxford, Oxford OX1 3RH, UK*
[6] *Astrobiology Center, NINS, 2-21-1 Osawa, Mitaka, Tokyo 181-8588, Japan*
[7] *National Astronomical Observatory of Japan, NINS, 2-21-1 Osawa, Mitaka, Tokyo 181-8588, Japan*

Downloaded from https://academic.oup.com/mnras/article/497/4/4423/5873020 by University College London user on 25 September 2020

[8]Department of Astrophysical Sciences, Princeton University, 4 Ivy Lane, Princeton, NJ 08544, USA
[9]Department of Physics and Kavli Institute for Astrophysics and Space Research, MIT, Cambridge, MA 02139, USA
[10]Chalmers University of Technology, Department of Space, Earth and Environment, Onsala Space Observatory, SE-439 92 Onsala, Sweden
[11]Leiden Observatory, University of Leiden, PO Box 9513, NL-2300 RA, Leiden, The Netherlands
[12]Las Cumbres Observatory, 6740 Cortona Dr., Ste. 102, Goleta, CA 93117, USA
[13]Rheinisches Institut für Umweltforschung an der Universität zu Köln, Aachener Strasse 209, D-50931 Köln, Germany
[14]Department of Astronomy, The University of Tokyo, 7-3-1 Hongo, Bunkyo-ku, Tokyo 113-0033, Japan
[15]Thüringer Landessternwarte Tautenburg, D-07778 Tautenburg, Germany
[16]Stellar Astrophysics Centre, Department of Physics and Astronomy, Aarhus University, Ny Munkegade 120, DK-8000 Aarhus C, Denmark
[17]Center for Astronomy and Astrophysics, TU Berlin, Hardenbergstr. 36, D-10623 Berlin, Germany
[18]Department of Astronomy and McDonald Observatory, University of Texas at Austin, 2515 Speedway, Austin, TX 78712, USA
[19]Center for Planetary Systems Habitability, University of Texas at Austin, Austin, TX 78730, USA
[20]Institute of Planetary Research, German Aerospace Center (DLR), Rutherfordstrasse 2, D-12489 Berlin, Germany
[21]Astronomical Institute, Czech Academy of Sciences, Fričova 298, CZ-25165 Ondřejov, Czech Republic
[22]Valencian International University (VIU), Pintor Sorolla 21, E-46002 Valencia, Spain
[23]Facultad de Ingeniería y Ciencias, Universidad Adolfo Ibánez, Av. Diagonal las Torres 2640, Peñalolén, Santiago, Chile
[24]Millennium Institute for Astrophysics, Av. Vicuña Mackenna 4860, 782-0436 Macul, Santiago, Chile
[25]Max-Planck-Institut für Astronomie, Königstuhl 17, D-69117 Heidelberg, Germany
[26]Instituto de Astrofísica, Pontificia Universidad Católica de Chile, Av. Vicuña Mackenna 4860, 782-0436 Macul, Santiago, Chile
[27]European Southern Observatory, Alonso de Córdova 3107, Vitacura, Casilla 19001, Santiago de Chile, Chile
[28]Astronomy Department and Van Vleck Observatory, Wesleyan University, Middletown, CT 06459, USA
[29]JST, PRESTO, 2-21-1 Osawa, Mitaka, Tokyo 181-8588, Japan
[30]Department of Earth, Atmospheric and Planetary Sciences, MIT, 77 Massachusetts Avenue, Cambridge, MA 02139, USA
[31]Institut de Ciències de l'Espai (ICE, CSIC), Campus UAB,C/ de Can Magrans s/n, E-08193 Bellaterra, Spain
[32]Institut d'Estudis Espacials de Catalunya (IEEC), C/ Gran Capitá 2-4, E-08034 Barcelona, Spain
[33]Department of Theoretical Physics and Astrophysics, Masaryk University, Kotlářská 2, CZ-61137 Brno, Czech Republic
[34]Astronomical Institute, Faculty of Mathematics and Physics, Charles University, Ke Karlovu 2027/3, CZ-12116 Prague, Czech Republic

This paper has been typeset from a TEX/LATEX file prepared by the author.

Downloaded from https://academic.oup.com/mnras/article/497/4/4423/5873020 by University College London user on 25 September 2020